Facet effect on the photoelectrochemical performance of a WO₃/BiVO₄ heterojunction photoanode

Yang Liu[a,b], Bryan R. Wygant[a], Kenta Kawashima[a], Oluwaniyi Mabayoje[a], Tae Eun Hong[a,c], Sang-Geul Lee[d], Jie Lin[a,e], Jun-Hyuk Kim[a,f], Kunio Yubuta[g], Wenzhang Li[b,*], Jie Li[b], C. Buddie Mullins[a,*]

[a] Department of Chemical Engineering and Department of Chemistry, University of Texas at Austin, Austin, TX, 78712-0231, United States
[b] College of Chemistry and Chemical Engineering, Central South University, Changsha, 410083, China
[c] Busan Center, Korea Basic Science Institute, Busan, 46742, Republic of Korea
[d] Daegu Center, Korea Basic Science Institute, Daegu, 41566, Republic of Korea
[e] College of Materials, Xiamen University, Xiamen, Fujian, 361005, China
[f] Research Institute of Industrial Science and Technology (RIST), Pohang, 37673, Republic of Korea
[g] Institute for Materials Research, Tohoku University, 2-1-1 Katahira, Aoba-ku, Sendai, 980-8577, Japan

ARTICLE INFO

ABSTRACT

Different WO₃ facets have different surface energies and electronic structures, and exhibit different water oxidation abilities and photocatalytic performance as a result. Because of the material's limited photoresponse region, loading a narrow bandgap material on WO₃ is a generally known method for improving photo-harvesting. In this paper, we have synthesized WO₃ films with different crystal facet ratios. After loading BiVO₄ on these WO₃ films, we measured the photoelectrochemical (PEC) performance to investigate the effects of WO₃ facet choice on the heterojunction film electrode's performance. We found that a high-intensity ratio of the (002) WO₃ facet in X-ray diffraction (XRD) leads to a more negative onset potential and higher photocurrents in a lower potential region. The ultraviolet photoelectron spectra show a lower work function for the 002-dominant WO₃ film compared to other WO₃ films, which may result in a higher quasi-fermi level for the heterojunction electrode. Based on the XRD results, the high-intensity ratio of the (002) WO₃ facet preferentially exposes the (020) BiVO₄ facet, which may be a reason for the better charge extraction observed at low applied potential and high faradic efficiency on PEC water splitting. Together, this results in a high hole injection efficiency for 002-dominant WO₃/BiVO₄ films compared with WO₃/BiVO₄ films favoring other WO₃ facet ratios.

1. Introduction

Photoelectrochemical (PEC) water splitting using semiconductor photoelectrodes is one of the most desirable and environmentally friendly methods to produce hydrogen from water using renewable solar energy, and it offers a promising approach for producing sustainable and renewable hydrogen fuel. Since the discovery of water splitting over TiO₂, semiconductor materials such as Fe₂O₃, WO₃, CdS, Bi₂WO₆, BiOIO₃ and BiVO₄, have been widely chosen for fabrication into photoelectrodes for PEC water splitting [1–6]. Of these, WO₃ is an attractive choice because it is an environmentally-friendly and low-cost material, has a moderate hole diffusion length of 150 nm, and an electron mobility of $12\,cm^2\,V^{-1}\,s^{-1}$ [7]. However, the photoresponse region of WO₃ is narrow because of its wide band gap (2.6–2.8 eV). It

limits the maximum photocurrent of WO₃ based photoanodes. To extend the photoresponse region and improve photoelectrochemical performance, enormous effort is being devoted to doping WO₃ with foreign elements or pairing with another semiconductor to construct a heterojunction.

Compared with other heterojunction photoanodes based on WO₃, WO₃/BiVO₄ is a good candidate for PEC water splitting [8–10]. Since Chatchai et al. [11] demonstrated a WO₃/BiVO₄ photoanode in 2009, this heterojunction has attracted tremendous attention. Hong et al. [12] fabricated WO₃/BiVO₄ electrodes using a layer-by-layer deposition method, and they demonstrated an optimal consisting of four layers of WO₃ covered by a single layer of BiVO₄. To improve the charge transport ability of BiVO₄, Mo was used as a foreign element for doping, and the resulting Mo-doped BiVO₄/WO₃ (WO₃/BiV₀.₉₅Mo₀.₀₅O₄)
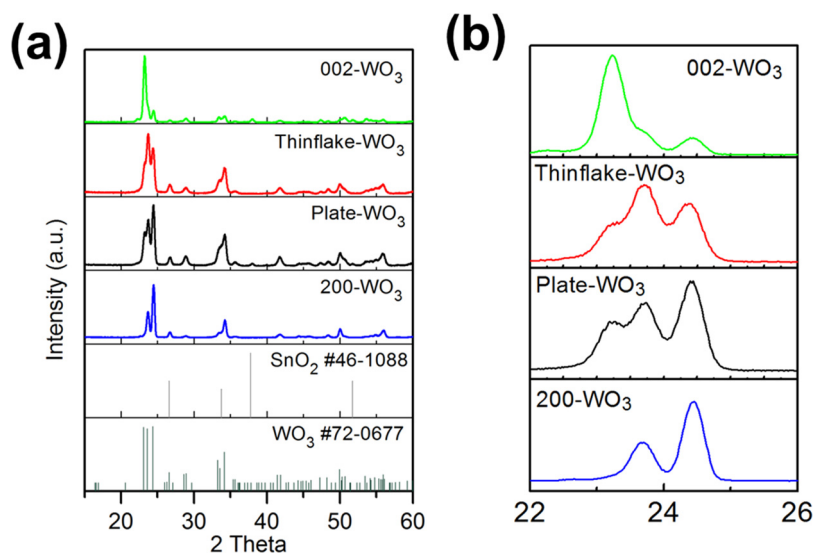

Fig. 1. (a) XRD patterns of WO₃ films, and (b) partially enlarged view of (a).

showed 1.5 times the photocurrent compared with the undoped WO₃/BiVO₄ heterojunction photoanode [13]. W-doped BiVO₄ was also used as an interlayer to enhance the PEC performance of WO₃/BiVO₄ heterojunctions [14]. Meanwhile, Sayama et al. introduced a very thin SnO₂ interlayer between WO₃ and BiVO₄, which improved the intrinsic quantum efficiency of the photocurrent generated from excited electrons in BiVO₄ [15]. Constructing suitable nanostructure or morphology is also a common route to obtaining high-performance WO₃/BiVO₄ heterojunction photoanode. Thus, one-dimensional WO₃/BiVO₄ electrodes [16–20], butterfly wing-like structures [21], inverse opal structure [22], and hierarchical nano-porous sphere arrays [23] have been fabricated in recent years. To investigate the effect of WO₃ morphology, Hwang et al. coated spherical-, rod-like- and plate-like-WO₃ via a doctor-blade method and loaded BiVO₄ on the WO₃ films. Though the spherical WO₃ didn't show the highest photocurrent of these three WO₃ photoanodes, it showed the highest photocurrent after loading BiVO₄ [24]. Aside from the difference in morphology, the spherical-WO₃ samples also had different peak intensity proportions for the (002), (020), and (200) peaks in XRD when compared with rod-like- and plate-like-WO₃. We also found different peak proportions when comparing the one-dimensional WO₃/BiVO₄ electrodes in other papers, all of which showed different PEC performance [16,18,19,25]. Some published papers have shown different water oxidation abilities for WO₃ samples with different exposed facets [26–28]. Such a facet adjustment should also affect the interface with other components and the corresponding PEC performance [29]. However, few papers have discussed this facet effect of WO₃ as related to the PEC performance of heterojunction electrodes. In one study, Dai et al. deposited silver nanoparticles onto WO₃ nanorods with different facets by an in situ photoreduction method [30]. The Ag/WO₃-110 catalysts with dominant exposed {001} facets exhibited better photocatalytic activity than Ag/WO₃-001 with a high percentage of exposed {100} and {010} facets.

In this paper, we have synthesized four different WO₃ films with various crystallographic orientations and exposed facets. We discuss possible reasons for the correlation between the PEC performance of a WO₃/BiVO₄ heterojunction photoanode and the structural characteristics of WO₃ with different crystallographic orientations or facets. X-ray diffraction (XRD) patterns and pole figures are used to determine the crystallographic orientations of these WO₃ films. Ultraviolet photoelectron spectroscopy (UPS) and valence band X-ray photoelectron spectroscopy (XPS) measurements were performed to investigate how the electronic structure changes in the heterojunction films.

2. Experimental section

2.1. Chemicals and materials

Tungstic Acid (H₂WO₄), sodium tungstate dihydrate (Na₂WO₄·2H₂O), poly(vinyl alcohol) (M.W. ≈ 86,000), bismuth(III) nitrate pentahydrate (Bi(NO)₃·5H₂O, 98%) and vanadyl acetylacetonate were purchased from Sigma-Aldrich. Hydrogen peroxide (30%), oxalic acid (C₂H₂O₄), urea, acetonitrile, and acetic acid were purchased from Fisher Chemicals. Hydrochloric acid (HCl) was obtained from VWR Inc. All the chemicals were used as received and deionized (DI) water (resistance ≈ 18.2 MΩ) was used throughout the experiments.

2.2. Fabrication of WO₃ thin-flake arrays on FTO

Thin-flake WO₃ arrays were grown onto a seed layer of WO₃ by a solvothermal method [31]. Firstly, the seed layer for the thin-flake film was deposited on FTO (2 cm × 3 cm) by spin coating a precursor solution (0.2 mL) at 2000 rpm for 18 s followed by annealing at 500 °C for 1 h in the air. This solution was prepared by dissolving 0.25 g of H₂WO₄ and 0.1 g of poly (vinyl alcohol) (PVA) in 3 mL of H₂O₂. Secondly, a H₂WO₄ (0.1 M) solution for the solvothermal step was prepared by dissolving 0.25 g of H₂WO₄ into a mixture of water (7 mL DI water) and H₂O₂ (3 mL) while heating at 95 °C on a hot plate with stirring. Thirdly, the seed-coated substrate was placed in a 20 mL Teflon-lined autoclave with active material side facing down when leaned against the wall. The precursor solution was prepared by adding 0.02 g of oxalic acid, 0.02 g of urea, 0.25 mL of HCl (12 M), 1.0 mL of DI water, and 2.0 mL of H₂WO₄ (0.1 M) solution (room temperature) into 12.5 mL of acetonitrile in sequence. Then the solution was transferred into the autoclave, and the reaction was kept at 180 °C for 2 h. Finally, the resulting films were washed with ethanol, air-dried at room temperature, and annealed in a muffle furnace at 500 °C for 1 h. These films are denoted as **thinflake-WO₃**. For comparison, two additional thin-flake films with different ratios of (002):(020):(200) X-ray diffraction (XRD) peaks were synthesized by changing the relative ratios of components in the precursor solutions (as shown in the Supporting Information).

2.3. Fabrication of 002-WO₃ film on FTO

A WO₃ film with a high 002 peak ratio in its XRD patterns was grown onto a 002 orientation seed layer using a hydrothermal method. The seed layer was prepared by following a prior report [17]. A
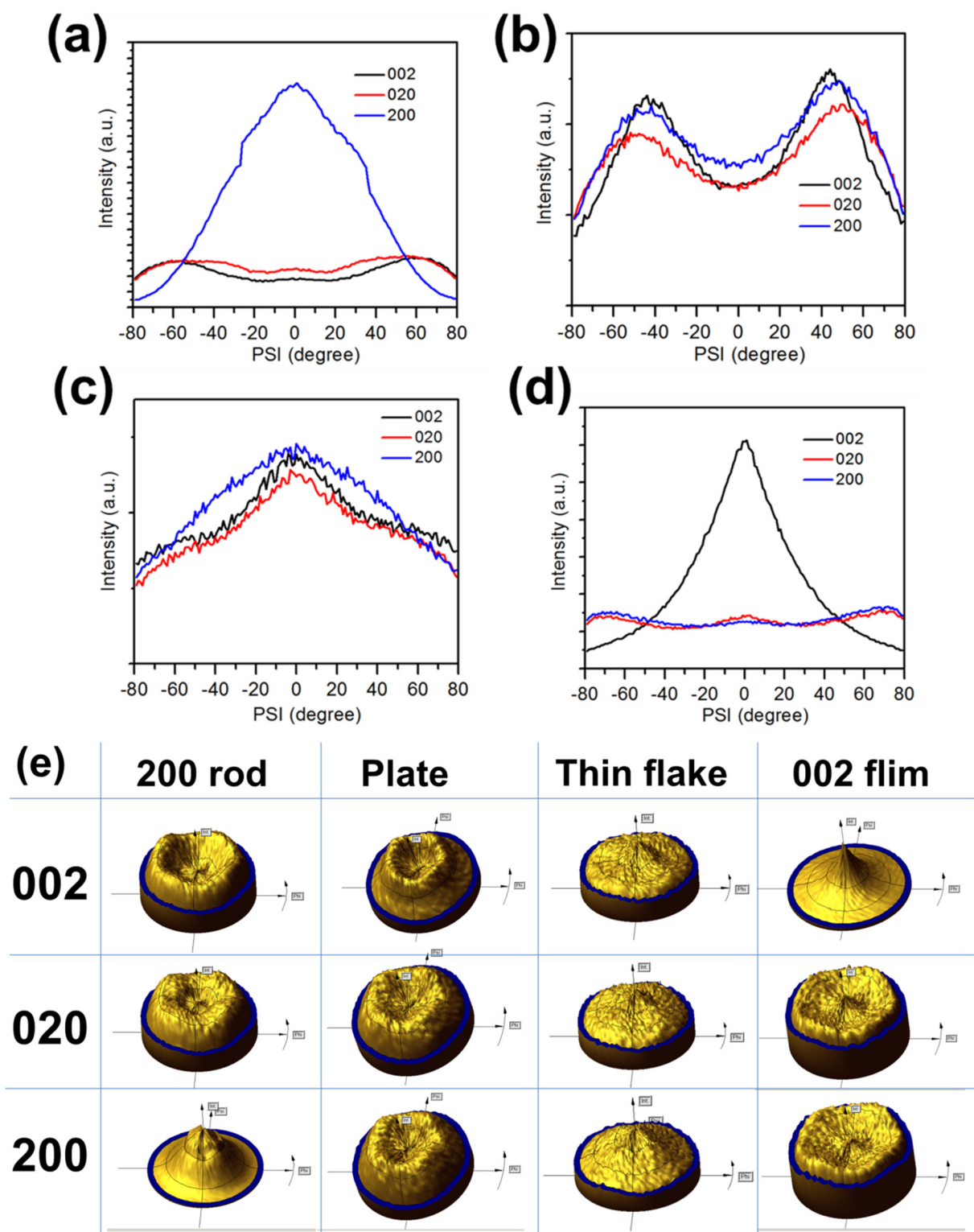
Fig. 2. The orientation distribution functions (ODFs) of (a) 200-WO$_3$, (b) plate-WO$_3$, (c) thinflake-WO$_3$ and (d) 002-WO$_3$; and (e) 2.5D pole figures of the (002), (020), (200) facets for the 200-WO$_3$, plate-WO$_3$, thinflake-WO$_3$ and 002-WO$_3$.

precursor solution was prepared by adding 0.188 g of tungstic acid and 1.44 g of citric acid into 75 mL of deionized water. After sonicating for 30 min, the solution was stirred for 1 day. The pH of the solution was adjusted to ˜1.5 by using concentrated hydrochloric acid. Then, the solution was transferred into a 20 mL hydrothermal autoclave with an FTO substrate with a 002 orientation seed layer placed face down and leaned against the wall. The sealed autoclave was kept in a furnace at

180 °C for 1 day. Finally, the sample was rinsed several times with DI water and subsequently heated at 500 °C for 1 h in the air; the final film is denoted as **002-WO$_3$**.

2.4. Fabrication of plate-like WO$_3$ arrays on FTO

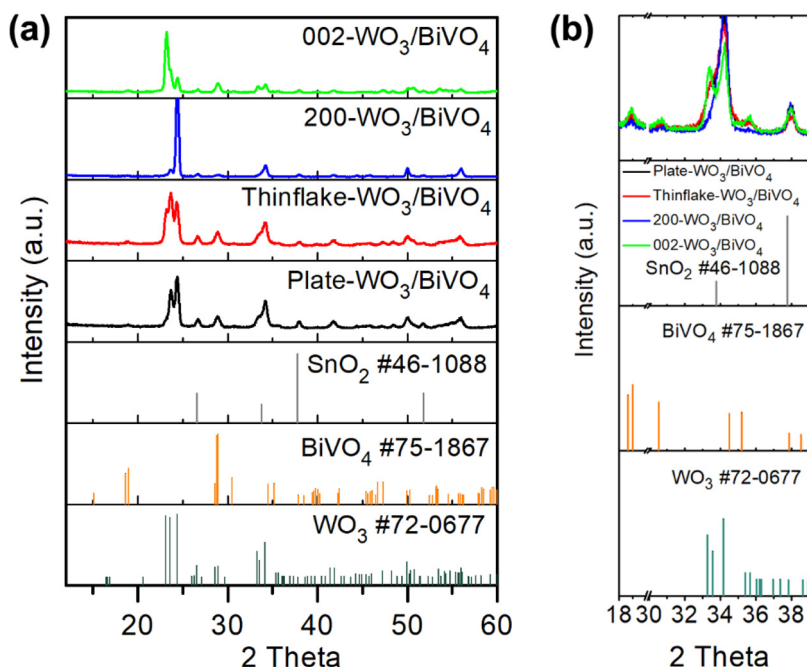Plate-like WO$_3$ arrays were grown directly onto FTO by a simple

Fig. 3. (a) XRD patterns of $WO_3/BiVO_4$ synthesized by spin coating, and (b) partially enlarged view of (a).

hydrothermal method. The FTO substrate was placed in a 20 mL Teflon-lined autoclave with the conductive surface facing down when leaned against the wall. A precursor solution was prepared by dissolving 0.056 g $Na_2WO_4 \cdot 2H_2O$ in 14 mL DI water and then adding 1.5 mL hydrochloric acid (12 M). After stirring for 10 min, 0.04 g oxalic acid and 0.01 g ammonium chloride were added to the solution. After further stirring for 20 min, the solution was added to the autoclave, and the reaction was kept at 150 °C for 6 h. Finally, the resulting films were washed with DI water, air-dried at room temperature, and annealed in a muffle furnace at 500 °C for 1 h, resulting in films denoted as **plate-WO₃**.

2.5. Fabrication of 200-WO₃ rod arrays on FTO

WO₃ rod arrays were grown directly onto FTO using a hydrothermal method [32]. The precursor solution was prepared by dissolving 0.15 g ammonium paratungstate in 15 mL DI water. Then, 0.6 mL 12 M HCl and 0.3 mL H_2O_2 were added into the solution. A clean FTO substrate with the conductive surface facing down was immersed in a 20 mL Teflon-lined autoclave filled with the precursor solution. After the hydrothermal process at 170 °C for 4 h, the resulting films were washed with DI water followed by air-drying at room temperature and then annealed in a muffle furnace at 500 °C for 1 h, resulting in films denoted as **200-WO₃**.

2.6. Fabrication of WO₃/BiVO₄ films

A BiVO₄ precursor solution was prepared by dissolving 0.051 g of Bi$(NO)_3 \cdot 5H_2O$ and 0.028 g vanadyl acetylacetonate in a mixed solvent of 2 mL acetic acid and 0.15 mL acetylacetone. This solution was used to create a thin BiVO₄ layer on top of the various WO₃ films. 20 μL of the solution was spin-coated on the WO₃ film (1 × 1.5 cm²) at 600 rpm for 5 s and 2000 rpm for 20 s. After drying at 200 °C for 10 min, the procedure was repeated 3 more times. Finally, the samples were annealed in a tube furnace at 500 °C for 1 h with a heating rate of 3 °C min⁻¹. For comparison, we also synthesized the composite films by drop casting with 12 mg/mL PEG in the same precursor solution.

2.7. Characterization

The crystalline structures of the samples were acquired with glancing-angle X-ray diffraction (XRD) patterns by Rigaku Ultima IV using Cu Kα radiation (λ = 0.15406 nm). The pole figures were measured with (002), (020) and (200) reflections of the WO₃ phase by using X'PERT PRO (PHILIPS, Netherlands). The psi was measured between 0° and 81° in steps of 3°. At each psi, a complete circle (0-360°) was measured in steps of 3°. The X'pert texture software (version 1.2) was used to calculate the pole figures. The morphology and microstructure were studied using a Quanta 650 FEG scanning electron microscope (SEM) and a JEOL 2010 F transmission electron microscope (TEM). For the WO₃/BiVO₄ samples with a high drop casting volume, the TEM and selected area electron diffraction (SAED) patterns were measured using an EM-002B (TOPCON) transmission electron microscope operated at 200 kV. Energy dispersive X-ray spectroscopy (EDS) of the SEM was used to determine the elemental composition of the samples. UV–vis absorption spectra were recorded in the range of 400–600 nm using a spectrophotometer (Cary 5000 UV–vis-NIR spectrometer) attached to an integrating sphere. The elemental composition was determined by an X-ray photoelectron spectroscopy (XPS, Kratos Axis Ultra spectrometer) using a monochromated Al Kα source. The XPS spectra are charge-corrected to the adventitious C 1s peak at 284.8 eV.

PEC measurements were performed using a three-electrode system. The as-prepared samples were used as working electrodes with exposed areas of approximately 0.20 cm². A Pt wire counter electrode and Ag/AgCl (saturated KCl) reference electrode were used. All the electrochemical tests were carried out on a CHI660D electrochemical workstation. The measured potential vs. Ag/AgCl was converted to the reversible hydrogen electrode (RHE) using the following equation:

$$E_{RHE} = E_{Ag/AgCl} + 0.0591 \times pH + E^o_{Ag/AgCl} \text{ (saturated KCl)} \quad (1)$$

where $E^o_{Ag/AgCl}$ (saturated KCl) = 0.197 V at 25 °C. A Newport 9600 solar simulator (150 W) with an air mass 1.5 (AM 1.5 G) filter was used as the illumination source, and the power density of it was calibrated to 100 mW cm⁻² using a thermopile detector.

The evolved O_2 by WO₃ based photoanodes were measured in a three-electrode cell using an oxygen sensor (Fox, Ocean Optics, type R) with the optical fiber inside a sealed glass tube inserted into 28 mL of
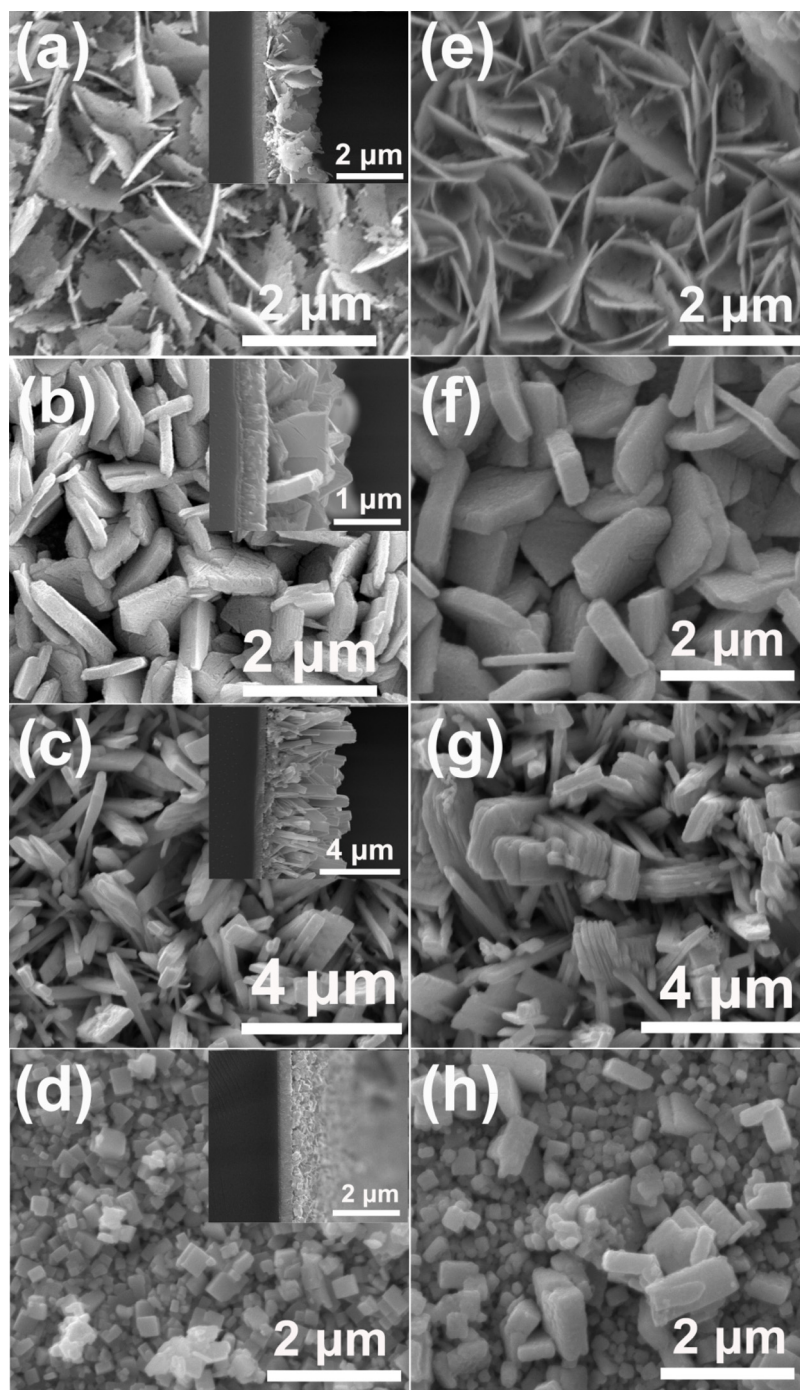
Fig. 4. Top and cross-sectional scanning electron microscope (SEM) images of (a) thinflake-WO$_3$, (b) plate-WO$_3$, (c) 200-WO$_3$, (d) 002-WO$_3$; top SEM images of spin coating WO$_3$/BiVO$_4$: (e) thinflake-WO$_3$/BiVO$_4$, (f) plate-WO$_3$/BiVO$_4$, (g) 200-WO$_3$/BiVO$_4$, and (h) 002-WO$_3$/BiVO$_4$.

0.5 M KPi solution. The salinity calibration value is 80 in this experiment. Each electrode was measured under an illumination intensity of ~200 mW cm^{-2} with AM 1.5 G filter and a bias of 1.23 V vs. RHE. The theoretical amount of oxygen output was calculated by the accumulated charge passed assuming 100% oxygen yield. Faradaic oxygen evolution efficiency was estimated by the actual generated amount and theoretical amount.

3. Results and discussion

The XRD patterns of WO$_3$ samples are shown in Fig. 1. Based on the characteristic peaks, monoclinic WO$_3$ (ICDD PDF# 72-0677) patterns

were obtained for all of the WO$_3$ films. The peaks at 2θ values of 23.1°, 23.6°, and 24.2° can be ascribed as the (002), (020), and (200) planes, respectively. The peak intensity profiles of 200-WO$_3$, plate-WO$_3$, 002-WO$_3$, and thinflake-WO$_3$ show different peak proportions. First, the most dominant peak in the XRD patterns of 200-WO$_3$ is the (200) peak. While the plate-WO$_3$ shows a lower intensity ratio (the intensity of peak/the sum intensity of (002), (020) and (200) peak) at (200) peak and higher intensity ratio at (020) peak than 200-WO$_3$, but the (200) peak is still the dominant peak. For thinflake-WO$_3$ and 002-WO$_3$, the dominant peaks are a (020) peak and a (002) peak, respectively. The area and normalized intensity ratios of different peaks are shown in Fig. S1. To further confirm the epitaxial orientation of the WO$_3$ samples,
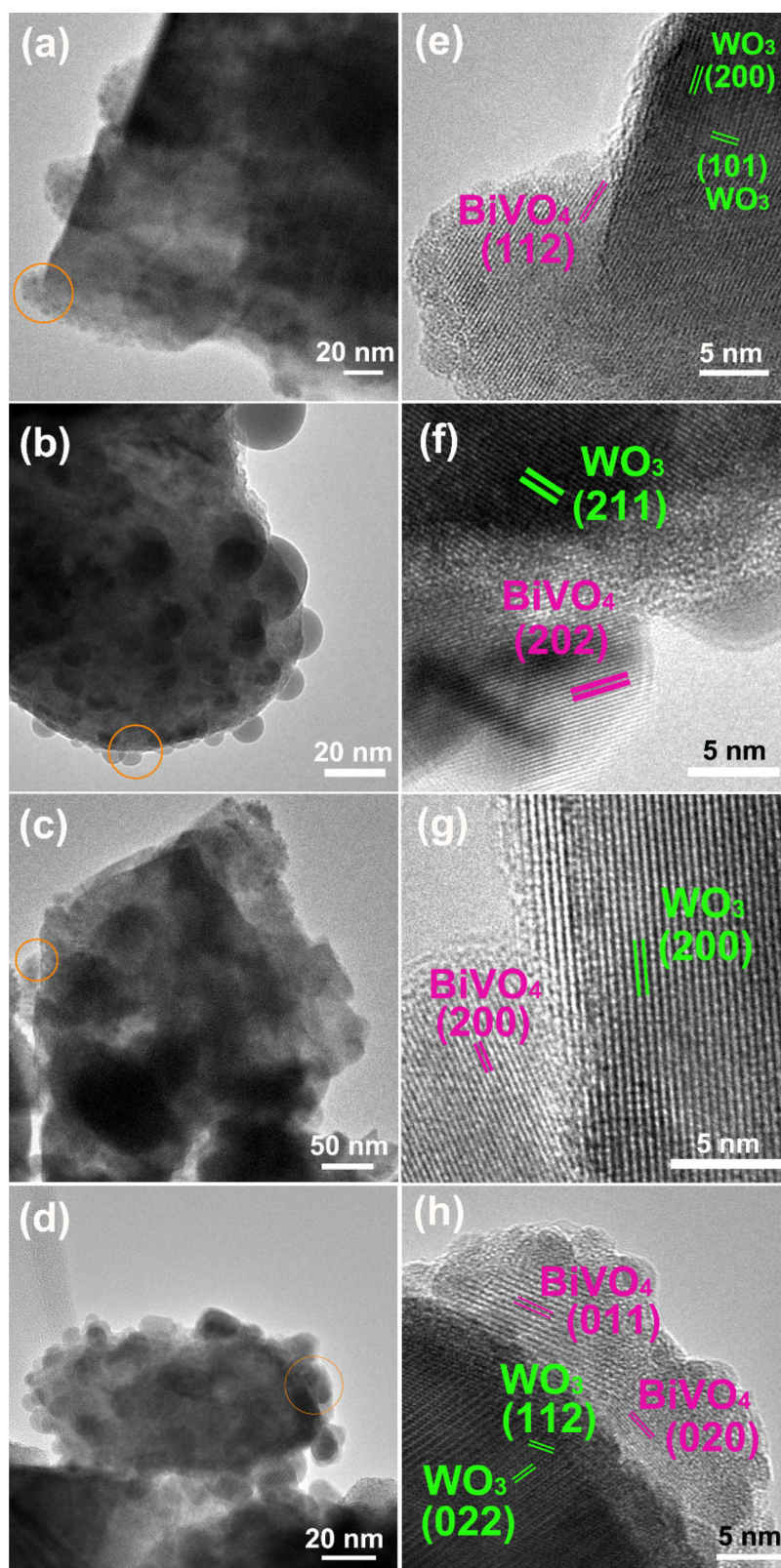
Fig. 5. Transmission electron microscope (TEM) images of (a) 200-WO$_3$/BiVO$_4$, (b) plate-WO$_3$/BiVO$_4$, (c) thinflake-WO$_3$/BiVO$_4$, (d) 002-WO$_3$/BiVO$_4$; and high-resolution TEM (HRTEM) images of (e) 200-WO$_3$/BiVO$_4$,(f) plate-WO$_3$/BiVO$_4$, (g) thinflake-WO$_3$/BiVO$_4$, (h) 002-WO$_3$/BiVO$_4$.

texture measurements were performed with pole figures (Fig. 2). The centered distribution of the (002), (020) and (200) planes are different for plate-WO$_3$, thinflake-WO$_3$, 200-WO$_3$ and 002-WO$_3$, respectively (Fig. 2a–d). The centered distribution of (200) planes at $\Psi = 0$

indicates the strong presence of (200) planes parallel to the substrate along the [200] direction or c-axis [33]. For 002-WO$_3$, the preferential growth orientation is along the [002] direction, which is consistent with the results in the XRD patterns. After loading BiVO$_4$, the
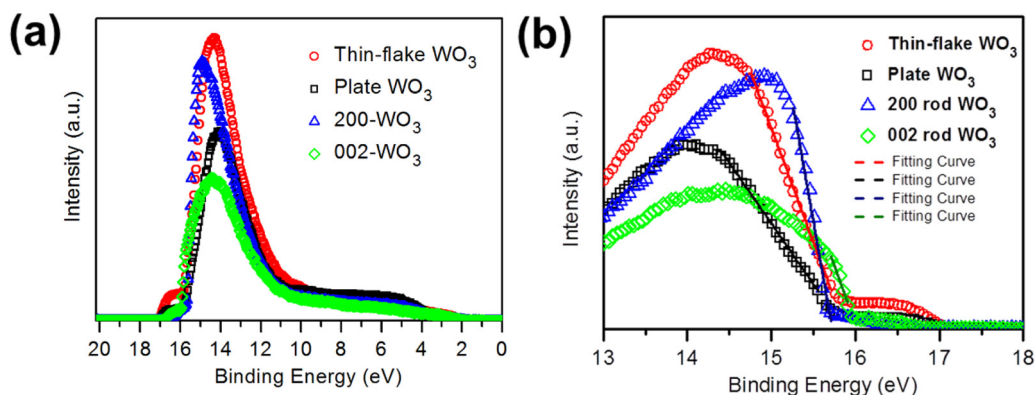
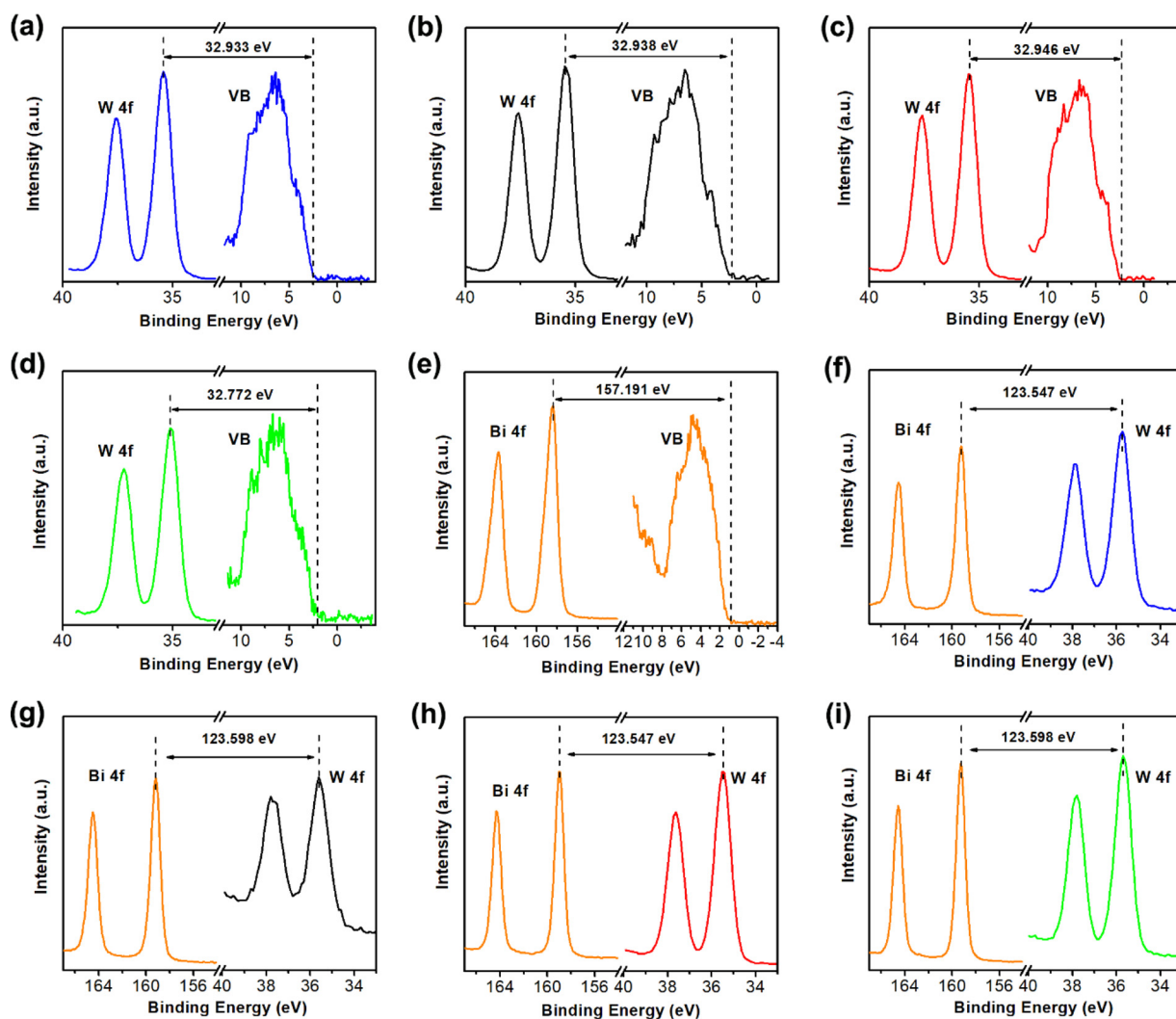**Fig. 6.** (a) Ultraviolet photoelectron spectra of WO$_3$, (b) partial magnification of (a).

Fig. 7. Energy difference between W 4f and VBM in (a) 200-WO$_3$, (b) plate-WO$_3$, (c) thinflake-WO$_3$, (d) 002-WO$_3$; (e) Energy difference between W 4f and VBM in the BiVO4, energy difference between Bi 4f and W 4f core levels in (f) 200-WO$_3$/BiVO$_4$, (g) plate-WO$_3$/BiVO$_4$, (h) thinflake-WO$_3$/BiVO$_4$, (i) 002-WO$_3$/BiVO$_4$.

characteristic peaks corresponding to WO$_3$ are nearly unchanged (Figs. 3a and S3a), while some new peaks appeared at 2θ = 18.7, 28.9 and 30.5° are associated with the (101), (112), and (004) planes of monoclinic BiVO$_4$ (PDF#75-1867), respectively. The 200-WO$_3$/BiVO$_4$ sample shows higher peak intensity than other samples at 2θ = 34.2 and 37.9°, which can be indexed to the (202) plane of monoclinic WO$_3$ (ICDD PDF#72-0677) and the (202) plane of monoclinic BiVO$_4$ (ICDD PDF#75-1867), respectively (Figs. 3b and S3b). Compared with 200-

WO$_3$/BiVO$_4$, plate-WO$_3$/BiVO$_4$ and thinflake-WO$_3$/BiVO$_4$ have a higher peak intensity at 2θ = 35.2° associated with the (020) plane of BiVO$_4$. In addition to the highest peak intensity at 2θ = 35.2°, the 002-WO$_3$/BiVO$_4$ has two additional peaks at 2θ = 33.3 and 34.6°, which can be indexed to the (022) plane of WO$_3$ and the (200) plane of BiVO$_4$. Our data clearly shows that the exposed facets of WO$_3$ affect the crystallization orientation of BiVO$_4$.

The SEM images reveal that the WO$_3$-thin flake, WO$_3$-plate, and

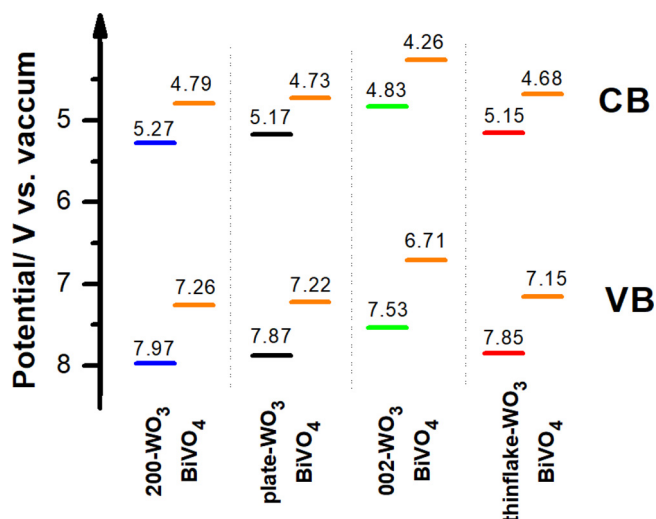**Fig. 8.** Calculated conduction band (CB) and valence band (VB) values of WO₃/BiVO₄ samples.

WO₃-rod show thin flake, plate-like, and rod morphology, respectively (Fig. 4). The cross-sectional SEM images (**inset of** Fig. 4) show that all of the WO₃ grow vertically on the FTO. After loading BiVO₄, the samples show slightly rougher surfaces (Figs. 4 and S4). The elemental mapping (Fig. S5) displays that the BiVO₄ particles are successfully

attached on the surface of the WO₃ photoanode. In the TEM images (Figures 5a/5b/5c/5d), BiVO₄ with small size particles can be found attached at the boundary of the WO₃ sample. The HRTEM image (Fig. 5e) of 200-WO₃/BiVO₄ displays lattice spacings of 0.367 and 0.308 nm, corresponding to the (200) plane of WO₃ and the (112) plane of monoclinic BiVO₄. In Fig. 5f, plate-WO₃/BiVO₄ displays the lattice spacing of 0.301 and 0.237 nm, corresponding to the (211) plane of WO₃ and the (202) plane of monoclinic BiVO₄. In Fig. 5g, the lattice space of 0.368 and 0.261 nm can be indexed to the (200) plane of WO₃ and the (200) plane of monoclinic BiVO₄, respectively. For 002-WO₃/BiVO₄ (Fig. 5h), the lattice spacings of 0.461, 0.250 and 0.307 nm can be assigned to the (011) plane of BiVO₄, the (020) plane of BiVO₄, and the (112) plane of WO₃. For the WO₃/BiVO₄ sample with a high drop casting volume, SEM (Fig. S6), low magnification TEM (Fig. S7) and selected area electron diffraction (SAED) patterns (Fig. S8) were also measured, which confirm the existence of BiVO₄ on the WO₃ films.

XPS was performed to elucidate the elemental composition of the samples. In the survey spectra (Fig. S10), the XPS peaks indicate that 200-WO₃, plate-WO₃, 002-WO₃, and thinflake-WO₃ contain W (32–40 eV), O (527–536 eV) and trace amounts of carbon (280–289 eV). After loading BiVO₄, all samples show signals for Bi (156–166 eV) and V (512–519 eV). We also measured the energy band alignment using ultraviolet photoelectron spectroscopy (UPS) spectra (Fig. 6). The Fermi energy (E_{FE}) was estimated from the following equation [34]:

$$E_{FE} = h\nu - E_{cutoff} \qquad (2)$$

where $h\nu = 21.2\,eV$ (He I source), E_{cutoff} is the onset of the secondary

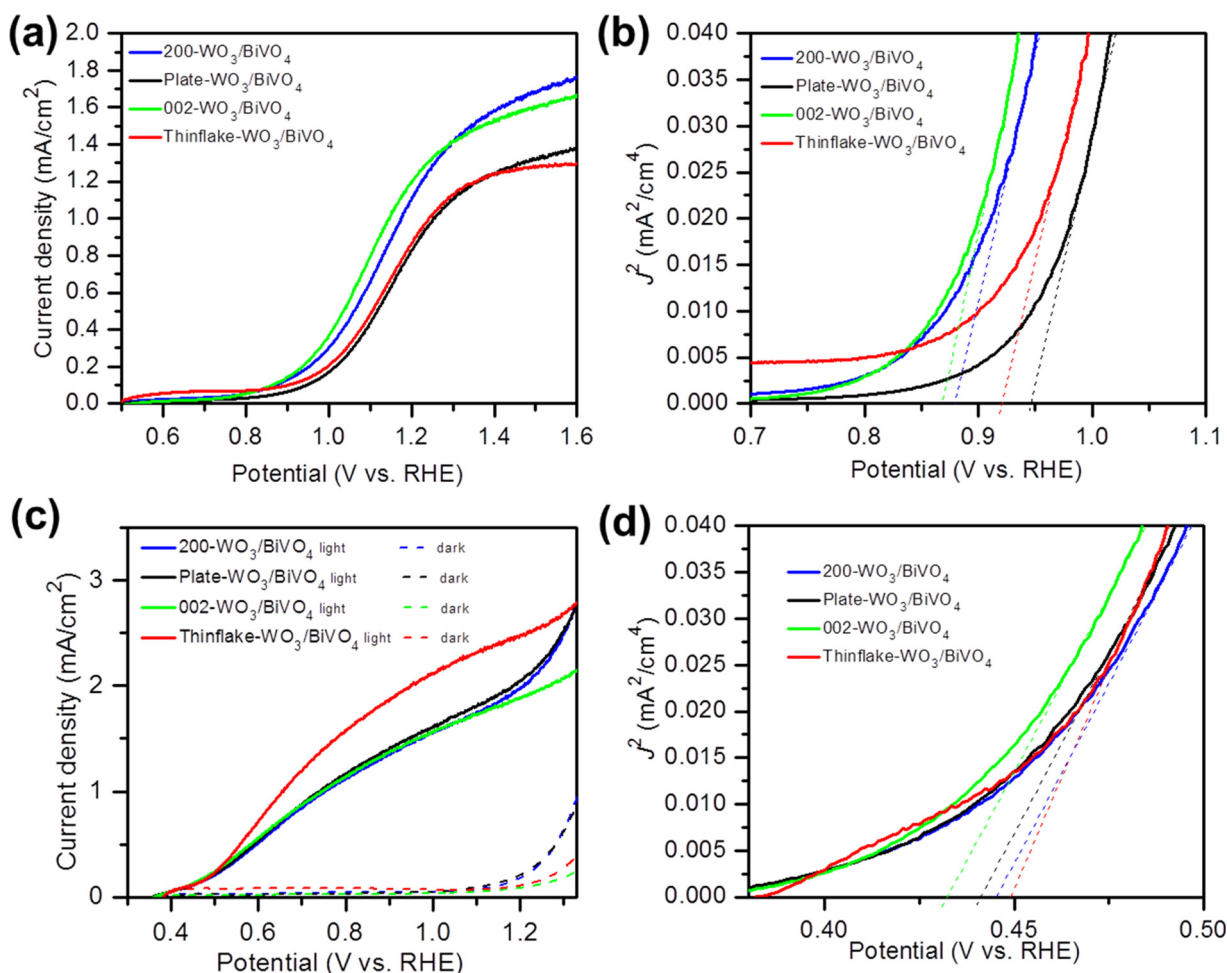**Fig. 9.** (a) Linear sweep voltammograms and (b) Bulter plots of spin coating WO₃/BiVO₄ measured in 0.5 M KPi (pH ≈ 7.2); (c) linear sweep voltammograms and (d) Bulter plots of spin coating WO₃/BiVO₄ measured in 0.5 M KPi + 0.5 M Na₂SO₃ (pH ≈ 7.5).
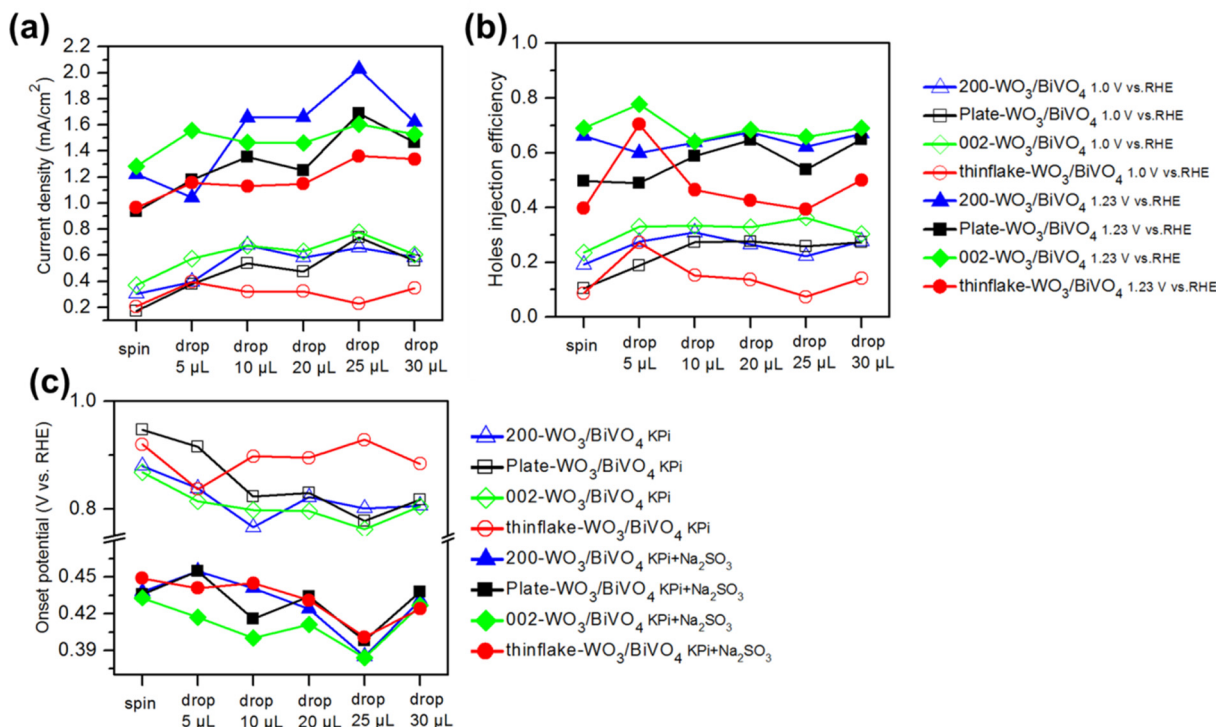
Fig. 10. (a) Photocurrent and (b) holes injection efficiency of spin coating (or drop casting) $WO_3/BiVO_4$; (c) onset potentials of $WO_3/BiVO_4$ measured in 0.5 M KPi and 0.5 M KPi + 0.5 M Na_2SO_3.
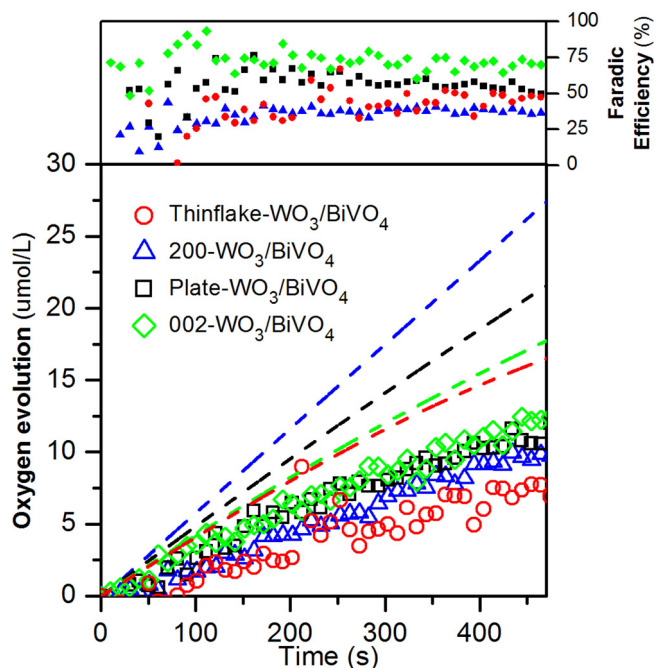

Fig. 11. Actual (open scatters) and theoretical (Dash line) oxygen evolution amount, and calculated Faradic efficiency (solid scatters).

emission.

As shown in Fig. 6b, the Fermi energy of 002-WO_3, plate-WO_3, thinflake-WO_3, and 200-WO_3 are 5.18, 5.33, 5.32 and 5.47 eV, respectively. The valence-band offset at the heterojunction interface was calculated by the following formula [35,36]:

$$\Delta\,E_V = (E_{Bi\,4f}^{WO3/BiVO4} - E_{W\,4f}^{WO3/BiVO4}) + (E_{W\,4f}^{WO3} - E_{VBM}^{WO3}) - (E_{Bi\,4f}^{BiVO4} - E_{VBM}^{BiVO4})$$

(3)

where $(E_{W\,4f}^{WO3} - E_{VBM}^{WO3})$ is the energy difference between the W 4f and VBM in the WO_3 film, $(E_{Bi\,4f}^{BiVO4} - E_{VBM}^{BiVO4})$ is the energy difference between the Bi 4f and VBM in the $BiVO_4$ film, $(E_{Bi\,4f}^{WO3/BiVO4} - E_{W\,4f}^{WO3/BiVO4})$ is the energy difference between the Bi 4f and W 4f core levels in the $WO_3/BiVO_4$ heterojunction. The core levels and valence band edge XPS spectra for WO_3, $BiVO_4$ and $WO_3/BiVO_4$ are shown in Fig. 7. WO_3 is an indirect transition semiconductor, and $BiVO_4$ is a direct transition semiconductor [37,38]. The band gap energies for the $WO_3/BiVO_4$ samples are estimated from $E_g = 1240/\lambda_{onset}$ instead of fitting Kubelka–Munk plots [39]. The bandgap values are 2.47, 2.49, 2.45, and 2.47 eV for 002-$WO_3/BiVO_4$, plate-$WO_3/BiVO_4$, thinflake-$WO_3/BiVO_4$, and 200-$WO_3/BiVO_4$, respectively. Because $BiVO_4$ instead of WO_3 has a photoresponse under light of wavelength around 500 nm, the calculated bandgap of 2.47, 2.49, 2.45, and 2.47 eV belong to the $BiVO_4$ in the $WO_3/BiVO_4$. Thus, the calculated conduction band potentials are shown in Fig. 8. Because the energy difference between the bottom of the conduction band and the Fermi level is about 0.2, 0.3 and 0.4 eV for 10^2, 10^3 and > 10^4 Ω cm in conductivity for oxide semiconductors, respectively [40], the estimated Fermi level values (vs. vacuum level) should follow the trends that 002-$WO_3/BiVO_4$ < thinflake-$WO_3/BiVO_4$ ≤ 200-$WO_3/BiVO_4$ ≤ plate-$WO_3/BiVO_4$. So, we can hypothesize that the different Fermi level of WO_3 on various facets affects the final Fermi level equilibration between WO_3 and the attached $BiVO_4$, which may affect the flat band potential in PEC measurements.

To better understand the relationship between the different facets of WO_3 and PEC performance of $WO_3/BiVO_4$, we tested the films for water splitting using simulated sunlight. For the spin coated samples, 002-$WO_3/BiVO_4$ had the highest photocurrent in the potential region between 0.8–1.2 V vs. RHE (Fig. 9a), indicating a better photo-generated charge extraction between WO_3 and $BiVO_4$. The onset potential of 002-$WO_3/BiVO_4$, extracted by extrapolating the linear part of the Butler plot ($J^2 - V$), is about 0.868 V vs. RHE (Fig. 9b). For plate-$WO_3/BiVO_4$, thinflake-$WO_3/BiVO_4$, and 200-$WO_3/BiVO_4$, it is about 0.945, 0.920, and 0.88 V vs. RHE, respectively. In the presence of 0.5 M Na_2SO_3 as the hole scavenger, the onset potentials of 002-$WO_3/BiVO_4$, plate-$WO_3/$
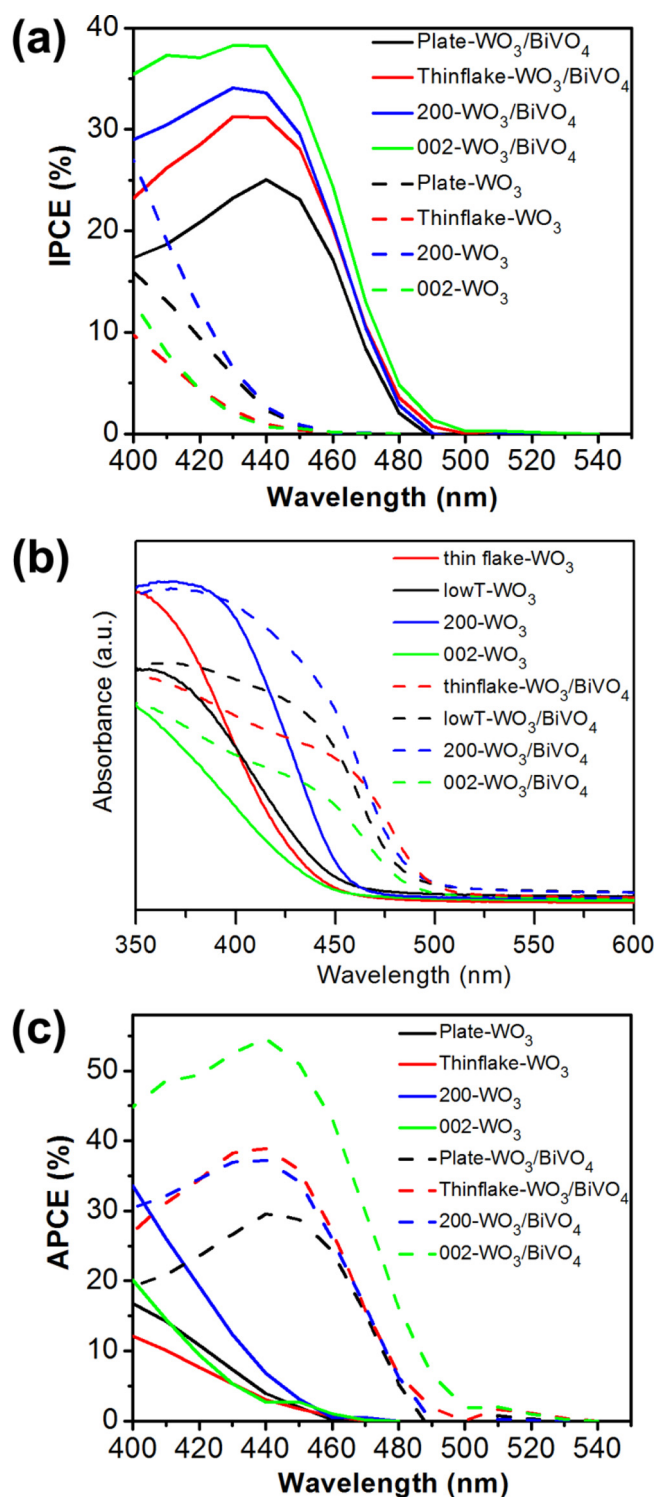
Fig. 12. (a) Incident photon to current conversion efficiency (IPCE), (b) UV–vis absorbance spectra, and (c) absorbed photon-to-current efficiency (APCE) of the samples.

BiVO$_4$, thinflake-WO$_3$/BiVO$_4$, and 200-WO$_3$/BiVO$_4$ are 0.433, 0.436, 0.447 and 0.438 V vs. RHE, respectively (Fig. 9c). When coating with BiVO$_4$ using the drop casting method (Fig. S11), 002-WO$_3$/BiVO$_4$ still shows the highest PEC performance at 1.0 V vs. RHE and the most negative onset potential of the four samples, indicating a better charge extraction between the 002 facet of WO$_3$ and BiVO$_4$. Due to the low electrochemical active surface area (Fig. S12), 002-WO$_3$ may have less surface area for BiVO$_4$ to disperse and form a thin, uniform layer on the

WO$_3$ compared with other WO$_3$ films. Thus, the photocurrent from the 002-WO$_3$/BiVO$_4$ sample is smaller than that of other films at 1.23 V vs. RHE when increasing the loading of BiVO$_4$. Additionally, band bending caused by the externally applied potential has a larger driving force to collect photogenerated electrons and oxidize water at 1.23 V (vs. RHE) than that at 1.0 V (vs. RHE). As a result, the driving force caused by the band offset between WO$_3$ and BiVO$_4$ becomes negligible. The effect of preferential orientation at the high applied potential (1.23 V vs. RHE) is not as evident as that at the low applied potential (1.0 V vs. RHE).

To investigate hole transfer ability, hole injection efficiency was obtained by measuring photocurrent in KPi with ($J_{\text{KPi} + \text{Na2SO3}}$) and without Na$_2SO_3$ (J_{KPi}), and calculating the efficiency using the following equations:

$$\eta = (J_{\text{KPi}})/(J_{\text{KPi} + \text{Na2SO3}}) \tag{4}$$

The 002-WO$_3$/BiVO$_4$ always had the highest hole injection efficiency for the four kinds of WO$_3$/BiVO$_4$ samples (Fig. 10b).

One possible reason for the more negative onset potential of 002-WO$_3$/BiVO$_4$, when compared with the other samples, is that the higher Fermi level for 002-WO$_3$ and corresponding crystallized BiVO$_4$ lead to a more negative Fermi level for the WO$_3$/BiVO$_4$ (Fig. 8). Additionally, 002-WO$_3$/BiVO$_4$ shows a preference for the 020 peak of BiVO$_4$ (Figs. 3b and S3b). Taken together, one interpretation for the improved performance we observe is that the photogenerated electrons are driven to the {010} facets of BiVO$_4$, which may then be easily transferred to WO$_3$ [41]. As a result, the photogenerated holes from BiVO$_4$ can be used to oxidize water instead of being quenched by photogenerated electrons [42]. Meanwhile, {010} facets of BiVO$_4$ present a lower energy barrier than the {110} facet in a Gibbs free-energy calculation [43]. Therefore, the {010} facets, and by extension the 020 facets, have a better potential for performing photoelectrochemical water oxidation. This may also be the reason for the high hole injection efficiency of 002-WO$_3$/BiVO$_4$.

The PEC water splitting performance of samples was surveyed in 0.5 M KPi electrolyte at 1.23 V vs. RHE. The 002-WO$_3$/BiVO$_4$ has highest actual oxygen evolution amount even though its theoretical value is not the largest (Fig. 11). The order of Faradic efficiency is 200-WO$_3$/BiVO$_4$ < thin-flake-WO$_3$/BiVO$_4$ < plate-WO$_3$/BiVO$_4$ < 002-WO$_3$/BiVO$_4$. It is same as the intensity of 020 peak trends (Fig. S13a). Meanwhile, it is interesting to note that the WO$_3$/BiVO$_4$ samples exhibit different electrochemical abilities in the oxidation of Na$_2$SO$_3$ under dark conditions. At 1.23 V vs. RHE, the order of dark current values in a 0.5 M KPi + 0.5 M Na$_2$SO$_3$ solution is 002-WO$_3$/BiVO$_4$ < thin-flake-WO$_3$/BiVO$_4$ < plate-WO$_3$/BiVO$_4$ ≤ 200-WO$_3$/BiVO$_4$ (Fig. 9c). It has similar trends as WO$_3$ (Fig. S14). Thus, the facet of WO$_3$ has effect on the valence band positions of WO$_3$/BiVO$_4$ and the oriented crystallization of BiVO$_4$, which lead to different oxidation abilities in various kind of electrolytes.

To further confirm the effect of the WO$_3$ facet orientation, 002-WO$_3$ and plate-WO$_3$ were coated with BiVO$_4$ by drop casting precursor solutions with different PEG concentrations in the precursor solution. Comparing these films with spin coated samples made without PEG in the precursor solution, it is readily apparent that the onset potential of both samples shifts negatively (Fig. S15). An increase of the 020 peak for BiVO$_4$ can also be seen in the XRD patterns, but after increasing the PEG concentration, the XRD patterns don't show any obvious changes (Fig. S16). The onset potential for 002-WO$_3$/BiVO$_4$ shifts negative slightly, while that of plate-WO$_3$/BiVO$_4$ shifts positive slightly, and 002-WO$_3$/BiVO$_4$ always show a more negative onset potential than plate-WO$_3$/BiVO$_4$. Meanwhile, the photocurrent and hole injection efficiency of 002-WO$_3$/BiVO$_4$ increases with increasing PEG concentration, and it is always higher than that of plate-WO$_3$/BiVO$_4$. Thus, increasing the preferential facet orientation (002) for WO$_3$ and the (020) facet for BiVO$_4$ is a useful strategy for getting negative onset potentials and great charge extraction between WO$_3$ and BiVO$_4$.
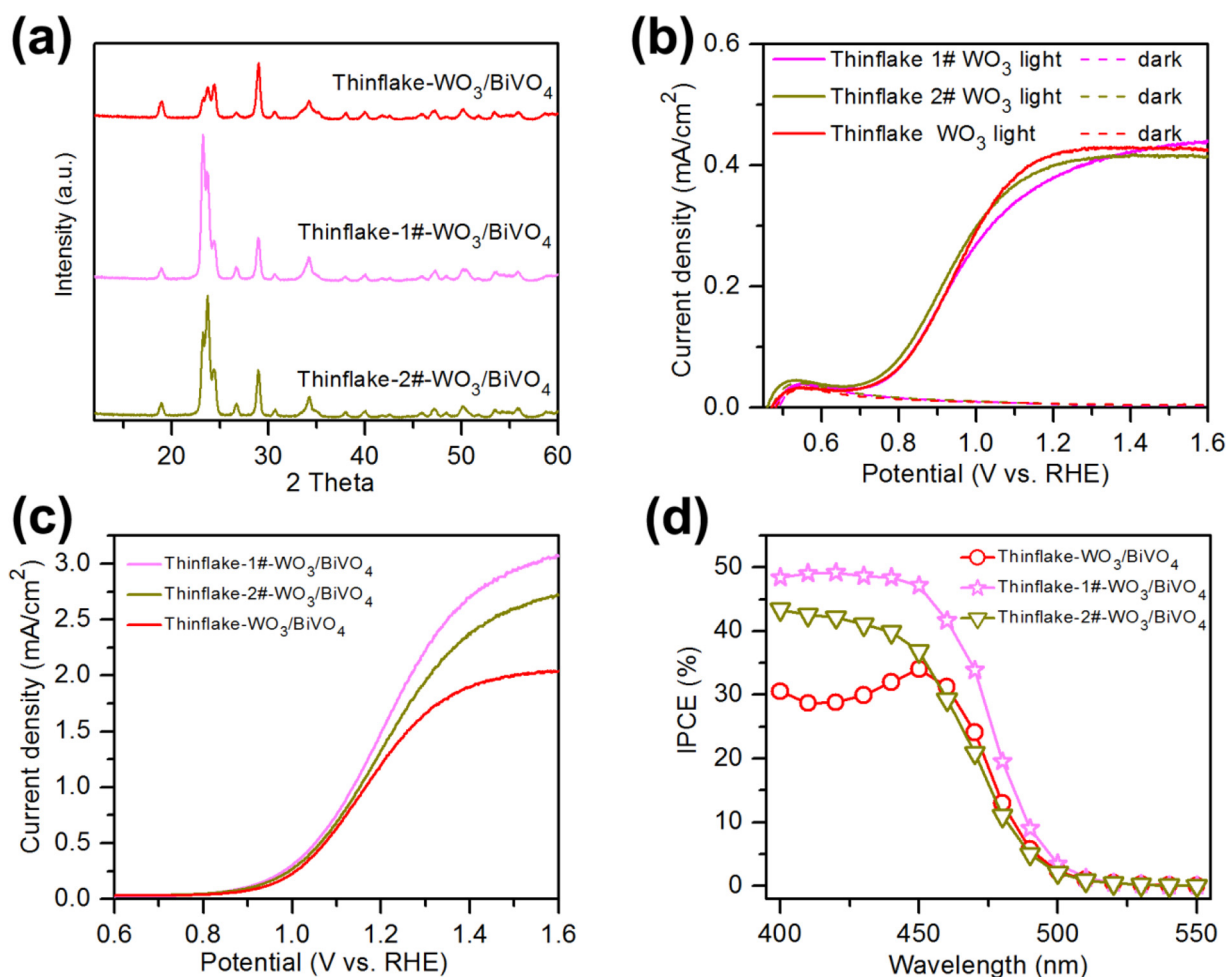
Fig. 13. (a) XRD patterns, (b) linear sweep voltammograms of WO_3, (c) linear sweep voltammograms of $WO_3/BiVO_4$, and (d) incident photon to current conversion efficiency (IPCE) of samples.

In order to monitor the ability of our electrodes to efficiently use the entire solar spectrum, incident photon-to-current efficiencies (IPCE) were measured and calculated according to the following equation [44]:

$$IPCE = (1240 \times I)/(\lambda \times J_{light}) \quad (5)$$

where I, λ, and J_{light} denote the photocurrent density, the incident light wavelength, and the measured irradiance, respectively.

All of the WO_3 films show photoelectrochemical ability at wavelengths less than ˜460 nm, while all of the $WO_3/BiVO_4$ films show performance at wavelengths less than ˜500 nm (Fig. 12a). We note that the $002\text{-}WO_3/BiVO_4$ heterojunction has a higher IPCE value than would be expected given the value for the $002\text{-}WO_3$ film. The optical absorption spectra of the samples (Fig. 12b) were also measured with a UV–vis absorption spectrometer. WO_3 films show photoabsorption in the UV and visible light regions, where the wavelength is shorter than 460 nm. After loading $BiVO_4$, the photoresponse region extends to ˜500 nm, which is consistent with the results in Fig. 12a. According to the above results, the absorbed photon-to-current efficiency (APCE) was calculated by dividing the IPCE by the light harvesting efficiencies (LHE) at each wavelength using the following equations [23]:

$$LHE = 1\text{–}10^{-A(\lambda)} \quad (6)$$

$$APCE = IPCE/LHE \quad (7)$$

where $A(\lambda)$ is the absorbance at a specific wavelength in UV–vis absorption spectra.

In Fig. 12c, it can be seen that $002\text{-}WO_3/BiVO_4$ sample has the highest APCE of the samples. When loading $BiVO_4$ via drop casting (Fig. S18), the IPCE values also increase for each sample relative to the bare WO_3. The limited increase in the IPCE values for $002\text{-}WO_3/BiVO_4$ may be caused by the small surface area of the $002\text{-}WO_3$ sample which cannot provide enough space for $BiVO_4$ to disperse and form a thin, uniform layer on. This may lead to an aggregation of $BiVO_4$ that will then lead to longer charge transfer distances. While this results in a slight decrease of the observed APCE values, the $002\text{-}WO_3/BiVO_4$ still shows higher APCE values when compared with other $WO_3/BiVO_4$ samples.

Based on the above results, a thinflake-WO_3 film with a high degree of 002 orientation (thinflake-1#-WO_3) was also synthesized (Figs. 13 and 14 and S19). In Fig. 13, the thinflake-1#-WO_3 has similar photocurrent as thinflake-WO_3, but the photocurrent and IPCE values of thinflake-1#-$WO_3/BiVO_4$ measured in KPi is much higher than that of thinflake-$WO_3/BiVO_4$. This indicates that controlling the crystallographic orientation of WO_3 is a valid method to enhance the PEC performance of WO_3 based heterojunction electrodes.

4. Conclusion

In conclusion, we successfully investigated the effect of WO_3 facet preference on the performance of $WO_3/BiVO_4$ heterojunctions. The WO_3 films with varied ratios of exposed facets were synthesized by different hydrothermal methods. The WO_3 film with higher ratios of the 002 facet showed the lowest work function, which leads to a higher
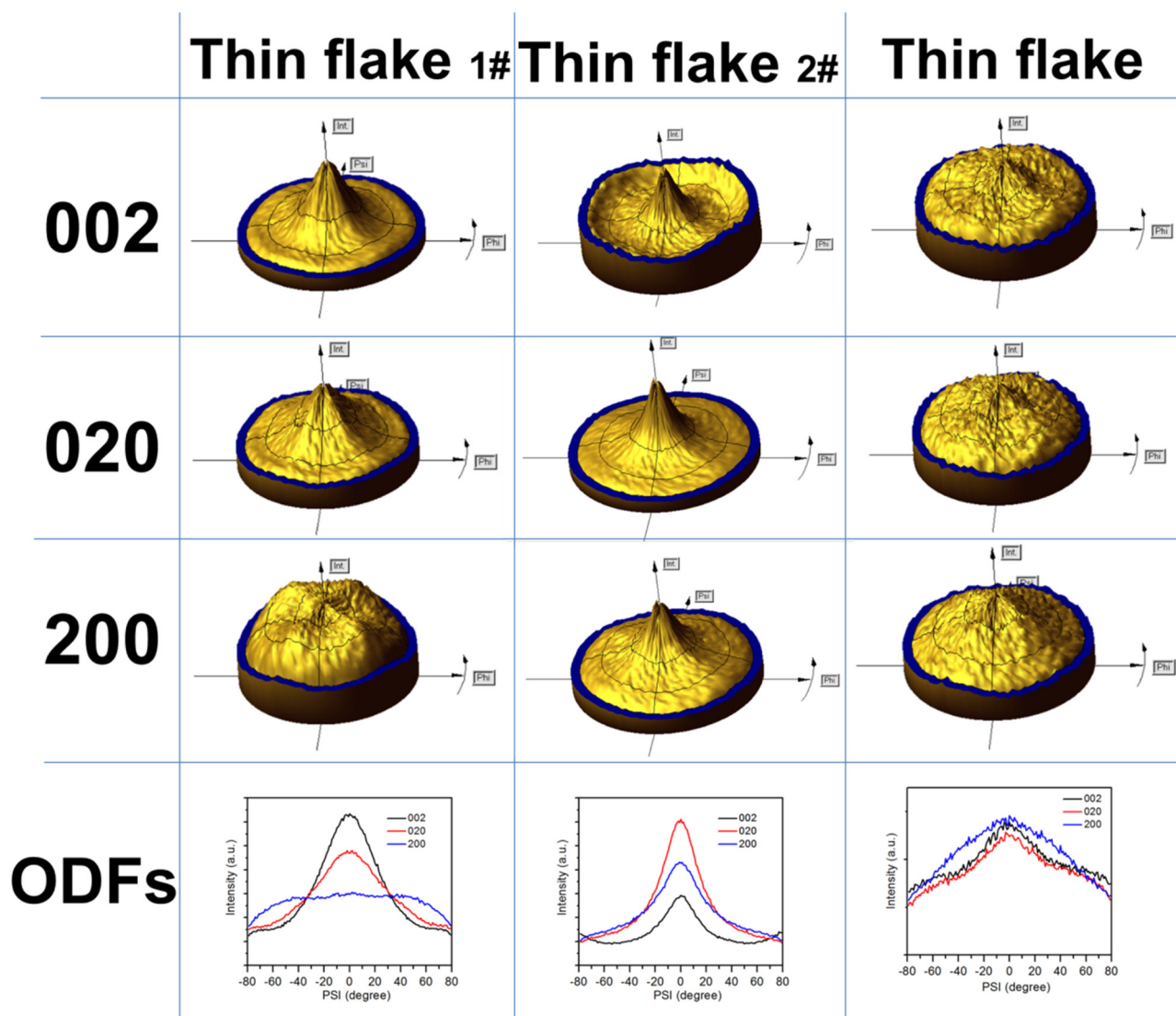
Fig. 14. 2.5D pole figures and orientation distribution functions (ODFs) of thinflake-1#-WO$_3$, thinflake-2#-WO$_3$, and thinflake-WO$_3$.

quasi-fermi level for the heterojunction film. The preferential facet orientation of WO$_3$ also affects the heteroepitaxial growth and facets of BiVO$_4$, which affect the onset potential and hole injection efficiency of the heterojunction film on water splitting in potassium phosphate buffer solution (pH $\approx$ 7). Because of the differences in energy level of WO$_3$/BiVO$_4$ and facets of BiVO$_4$, these samples also exhibit different oxidation abilities on PEC water splitting and electrocatalysis of Na$_2$SO$_3$. By controlling the crystallographic orientation of the WO$_3$ films, PEC performance can be tuned in the WO$_3$/BiVO$_4$ heterojunction electrodes.

Acknowledgements

Appendix A. Supplementary data

Supplementary material related to this article can be found, in the online version, at doi:https://doi.org/10.1016/j.apcatb.2018.12.058.

References

[1] A. Fujishima, K. Honda, Electrochemical photolysis of water at a semiconductor electrode, Nature 238 (1972) 37–38.
[2] S. Wang, P. Chen, Y. Bai, J.H. Yun, G. Liu, L. Wang, New BiVO$_4$ dual photoanodes with enriched oxygen vacancies for efficient solar-driven water splitting, Adv. Mater. 30 (2018) 1800486.
[3] S. Chen, J. Li, J. Bai, L. Xia, Y. Zhang, L. Li, Q. Xu, B. Zhou, Electron blocking and hole extraction by a dual-function layer for hematite with enhanced photoelectrocatalytic performance, Appl. Catal. B: Environ. 237 (2018) 175–184.
[4] R.-B. Wei, Z.-L. Huang, G.-H. Gu, Z. Wang, L. Zeng, Y. Chen, Z.-Q. Liu, Dual-cocatalysts decorated rimous CdS spheres advancing highly-efficient visible-light photocatalytic hydrogen production, Appl. Catal. B: Environ. 231 (2018) 101–107.
[5] H. Huang, R. Cao, S. Yu, K. Xu, W. Hao, Y. Wang, F. Dong, T. Zhang, Y. Zhang, Single-unit-cell layer established Bi$_2$WO$_6$ 3D hierarchical architectures: efficient adsorption, photocatalysis and dye-sensitized photoelectrochemical performance, Appl. Catal. B: Environ. 219 (2017) 526–537.
[6] F. Chen, H. Huang, Y. Zhang, T. Zhang, Achieving UV and visible-light photocatalytic activity enhancement of AgI/BiOIO$_3$ heterostructure: decomposition for diverse industrial contaminants and high mineralization ability, Chinese Chem. Lett. 28 (2017) 2244–2250.
[7] B.S. Kalanoor, H. Seo, S.S. Kalanur, Recent developments in photoelectrochemical water-splitting using WO$_3$/BiVO$_4$ heterojunction photoanode: a review, Mater. Sci.

Energy Technol. 1 (2018) 49–62.

[8] C. Liu, Y. Yang, J. Li, S. Chen, W. Li, X. Tang, An in situ transformation approach for fabrication of BiVO₄/WO₃ heterojunction photoanode with high photoelectrochemical activity, Chem. Eng. J. 326 (2017) 603–611.

[9] K. Yuan, Q. Cao, X. Li, H.-Y. Chen, Y. Deng, Y.-Y. Wang, W. Luo, H.-L. Lu, D.W. Zhang, Synthesis of WO₃@ZnWO₄@ZnO-ZnO hierarchical nanocactus arrays for efficient photoelectrochemical water splitting, Nano Energy 41 (2017) 543–551.

[10] T.H. Do, C. Nguyen Van, K.-A. Tsai, L.T. Quynh, J.-W. Chen, Y.-C. Lin, Y.-C. Chen, W.-C. Chou, C.-L. Wu, Y.-J. Hsu, Y.-H. Chu, Superior photoelectrochemical activity of self-assembled NiWO₄–WO₃ heteroepitaxy, Nano Energy 23 (2016) 153–160.

[11] P. Chatchai, Y. Murakami, S.-y. Kishioka, A.Y. Nosaka, Y. Nosaka, Efficient photocatalytic activity of water oxidation over WO₃/BiVO₄ composite under visible light irradiation, Electrochim. Acta 54 (2009) 1147–1152.

[12] S.J. Hong, S. Lee, J.S. Jang, J.S. Lee, Heterojunction BiVO4/WO₃ electrodes for enhanced photoactivity of water oxidation, Energy Environ. Sci. 4 (2011) 1781–1787.

[13] K. Zhang, X.-J. Shi, J.K. Kim, J.H. Park, Photoelectrochemical cells with tungsten trioxide/Mo-doped BiVO₄ bilayers, Phys. Chem. Chem. Phys. 14 (2012) 11119–11124.

[14] J. Choi, P. Sudhagar, J.H. Kim, J. Kwon, J. Kim, C. Terashima, A. Fujishima, T. Song, U. Paik, WO₃/W:BiVO₄/BiVO₄ graded photoabsorber electrode for enhanced photoelectrocatalytic solar light driven water oxidation, Phys. Chem. Chem. Phys. 19 (2017) 4648–4655.

[15] R. Saito, Y. Miseki, K. Sayama, Highly efficient photoelectrochemical water splitting using a thin film photoanode of BiVO₄/SnO₂/WO₃ multi-composite in a carbonate electrolyte, Chem. Commun. 48 (2012) 3833–3835.

[16] Y. Pihosh, I. Turkevych, K. Mawatari, T. Asai, T. Hisatomi, J. Uemura, M. Tosa, K. Shimamura, J. Kubota, K. Domen, T. Kitamori, Nanostructured WO₃/BiVO₄ photoanodes for efficient photoelectrochemical water splitting, Small 10 (2014) 3692–3699.

[17] J.-R. Ding, K.-S. Kim, 1-d WO₃@BiVO₄ heterojunctions with highly enhanced photoelectrochemical performance, Chem. Eng. J. 334 (2018) 1650–1656.

[18] M.G. Lee, D.H. Kim, W. Sohn, C.W. Moon, H. Park, S. Lee, H.W. Jang, Conformally coated BiVO₄ nanodots on porosity-controlled WO₃ nanorods as highly efficient type II heterojunction photoanodes for water oxidation, Nano Energy 28 (2016) 250–260.

[19] Y. Pihosh, I. Turkevych, K. Mawatari, J. Uemura, Y. Kazoe, S. Kosar, K. Makita, T. Sugaya, T. Matsui, D. Fujita, M. Tosa, M. Kondo, T. Kitamori, Photocatalytic generation of hydrogen by core-shell WO₃/BiVO₄ nanorods with ultimate water splitting efficiency, Sci. Rep. 5 (2015) 11141.

[20] P.M. Rao, L. Cai, C. Liu, I.S. Cho, C.H. Lee, J.M. Weisse, P. Yang, X. Zheng, Simultaneously efficient light absorption and charge separation in WO₃/BiVO₄ core/shell nanowire photoanode for photoelectrochemical water oxidation, Nano Lett. 14 (2014) 1099–1105.

[21] C. Yin, S.M. Zhu, D. Zhang, 3D nanostructured WO₃/BiVO₄ heterojunction derived from Papilio paris for efficient water splitting, RSC Adv. 7 (2017) 27354–27360.

[22] M. Ma, X. Shi, K. Zhang, S. Kwon, P. Li, J.K. Kim, T.T. Phu, G.-R. Yi, J.H. Park, A 3D triple-deck photoanode with a strengthened structure integrality: enhanced photoelectrochemical water oxidation, Nanoscale 8 (2016) 3474–3481.

[23] Y. Zhou, L. Zhang, L. Lin, B.R. Wygant, Y. Liu, Y. Zhu, Y. Zheng, C.B. Mullins, Y. Zhao, X. Zhang, G. Yu, Highly efficient photoelectrochemical water splitting from hierarchical WO₃/BiVO₄ nanoporous sphere arrays, Nano Lett. 17 (2017) 8012–8017.

[24] S.Y. Chae, C.S. Lee, H. Jung, O.-S. Joo, B.K. Min, J.H. Kim, Y.J. Hwang, Insight into charge separation in WO₃/BiVO₄ heterojunction for solar water splitting, ACS Appl. Mater. Interfaces 9 (2017) 19780–19790.

[25] J. Su, L. Guo, N. Bao, C.A. Grimes, Nanostructured WO₃/BiVO₄ heterojunction films for efficient photoelectrochemical water splitting, Nano Lett. 11 (2011) 1928–1933.

[26] R. Lin, J. Wan, Y. Xiong, K. Wu, W.-c. Cheong, G. Zhou, D. Wang, Q. Peng, C. Chen, Y. Li, A quantitative study of charge carrier dynamics in well-defined WO₃ nanowires and nanosheets: insight into the crystal facet effect in photocatalysis, J. Am. Chem. Soc. 140 (2018) 9078–9082.

[27] S. Wang, H. Chen, G. Gao, T. Butburee, M. Lyu, S. Thaweesak, J.-H. Yun, A. Du, G. Liu, L. Wang, Synergistic crystal facet engineering and structural control of WO₃ films exhibiting unprecedented photoelectrochemical performance, Nano Energy 24 (2016) 94–102.

[28] J. Zhang, P. Zhang, T. Wang, J. Gong, Monoclinic WO3 nanomultilayers with preferentially exposed (002) facets for photoelectrochemical water splitting, Nano Energy 11 (2015) 189–195.

[29] X. An, Y. Wang, J. Lin, J. Shen, Z. Zhang, X. Wang, Heterojunction: important strategy for constructing composite photocatalysts, Sci. Bull. 62 (2017) 599–601.

[30] J. Ding, L. Zhang, Q. Liu, W.-L. Dai, G. Guan, Synergistic effects of electronic structure of WO₃ nanorods with the dominant {001} exposed facets combined with silver size-dependent on the visible-light photocatalytic activity, Appl. Catal. B: Environ. 203 (2017) 335–342.

[31] J. Su, X. Feng, J.D. Sloppy, L. Guo, C.A. Grimes, Vertically aligned WO₃ nanowire arrays grown directly on transparent conducting oxide coated glass: synthesis and photoelectrochemical properties, Nano Lett. 11 (2010) 203–208.

[32] S.S. Kalanur, Y.J. Hwang, S.Y. Chae, O.S. Joo, Facile growth of aligned WO₃ nanorods on FTO substrate for enhanced photoanodic water oxidation activity, J. Mater. Chem. A 1 (2013) 3479–3488.

[33] J.Y. Zheng, A.U. Pawar, C.W. Kim, Y.J. Kim, Y.S. Kang, Highly enhancing photoelectrochemical performance of facilely-fabricated Bi-induced (002)-oriented WO₃ film with intermittent short-time negative polarization, Appl. Catal. B: Environ. 233 (2018) 88–98.

[34] J. Liu, Y. Liu, N. Liu, Y. Han, X. Zhang, H. Huang, Y. Lifshitz, S.-T. Lee, J. Zhong, Z. Kang, Metal-free efficient photocatalyst for stable visible water splitting via a two-electron pathway, Science 347 (2015) 970–974.

[35] J.-S. Liu, M. Clavel, M.K. Hudait, Tailoring the valence band offset of Al₂O₃ on epitaxial GaAs₁₋ySb_y with tunable antimony composition, ACS Appl. Mater. Interfaces 7 (2015) 28624–28631.

[36] Z.-G. Yang, L.-P. Zhu, Y.-M. Guo, W. Tian, Z.-Z. Ye, B.-H. Zhao, Valence-band offset of p-NiO/n-ZnO heterojunction measured by X-ray photoelectron spectroscopy, Phys. Lett. A 375 (2011) 1760–1763.

[37] J. Cao, B. Luo, H. Lin, B. Xu, S. Chen, Thermodecomposition synthesis of WO₃/H₂WO₄ heterostructures with enhanced visible light photocatalytic properties, Appl. Catal. B: Environ. 111–112 (2012) 288–296.

[38] N. Zhang, C. Chen, Z. Mei, X. Liu, X. Qu, Y. Li, S. Li, W. Qi, Y. Zhang, J. Ye, V.A.L. Roy, R. Ma, Monoclinic tungsten oxide with {100} facet orientation and tuned electronic band structure for enhanced photocatalytic oxidations, ACS Appl. Mater. Interfaces 8 (2016) 10367–10374.

[39] R.A.Z. Razera, H.I. Boudinov, F.S.B. Rodrigues, R.Z. Ferreira, A.F. Feil, Anomalous current–voltage behavior in Al/TiO2/n-Si structures, Phys. Status Solidi (RRL) – Rapid Res. Lett. 12 (2018) 1800057.

[40] U.K. Kirner, K.D. Schierbaum, W. Göpel, Interface-reactions of Pt/TiO₂: comparative electrical, XPS-, and AES-depth profile investigations, Freseniu's J. Anal. Chem. 341 (1991) 416–420.

[41] R. Li, F. Zhang, D. Wang, J. Yang, M. Li, J. Zhu, X. Zhou, H. Han, C. Li, Spatial separation of photogenerated electrons and holes among {010} and {110} crystal facets of BiVO₄, Nat. Commun. 4 (2013) 1432.

[42] H.L. Tan, X. Wen, R. Amal, Y.H. Ng, BiVO₄ {010} and {110} relative exposure extent: governing factor of surface charge population and photocatalytic activity, J. Phys. Chem. Lett. 7 (2016) 1400–1405.

[43] P.A. Kohl, S.N. Frank, A.J. Bard, Semiconductor electrodes XI. Behavior of n- and p-type single crystal semconductors covered with thin films, J. Electrochem. Soc. 124 (1977) 225–229.

[44] R.-B. Wei, P.-Y. Kuang, H. Cheng, Y.-B. Chen, J.-Y. Long, M.-Y. Zhang, Z.-Q. Liu, Plasmon-enhanced photoelectrochemical water splitting on gold nanoparticle decorated ZnO/CdS nanotube arrays, ACS Sustain. Chem. Eng. 5 (2017) 4249–4257.